Research Square

Preprints are preliminary reports that have not undergone peer review.
They should not be considered conclusive, used to inform clinical practice,
or referenced by the media as validated information.

Micro-Energy Characteristics and Their Relationships with Local Mechanical Mechanisms during Rock Mass Failure Development Abstract

Yu-Chen Wu
National Yang Ming Chiao Tung University
Chia-Ming Lo
cmlo@nctu.edu.tw

National Yang Ming Chiao Tung University

Research Article

Keywords: micro-energy signals, energy evolution, rock mass failure, local mechanical mechanisms

Posted Date: November 18th, 2026

DOI: https://doi.org/10.21203/rs.3.rs-11645768/v1

License: This work is licensed under a Creative Commons Attribution 4.0 International License.
Read Full License

Additional Declarations: No competing interests reported.

Micro-Energy Characteristics and Their Relationships with Local Mechanical Mechanisms during Rock Mass Failure Development
Abstract

Yu-Chen Wu, Chia-Ming Lo*

Department of Civil Engineering, National Yang Ming Chiao Tung University, Taiwan, R.O.C.

*Corresponding Author: cmlo@nctu.edu.tw

Abstract

This study aims to investigate the micro-energy characteristics during rock mass failure development and their relationships with local mechanical mechanisms. Micro-energy is defined as the energy within a local region of a rock mass. Three numerical models were established using the Discrete Element Method (DEM): a uniaxial compression test model, a direct shear test model, and a simplified slope model. Micro-energy signals were collected at selected particle-based monitoring points. Five types of micro-energy signals were analyzed: micro-strain energy, micro-bond strain energy, micro-friction energy, micro-damping energy, and micro-kinetic energy. The models were divided into failure development stages and spatial zones based on their mechanical and spatial characteristics. Five statistical indicators were then used to analyze the micro-energy signal characteristics across different stages and zones. The results reveal clear differences in micro-energy characteristics across failure development stages and spatial locations, as well as close relationships between different micro-energy types and specific local mechanical mechanisms. Comparisons among the three models demonstrate that different mechanical behaviors exhibit distinct micro-energy characteristics, helping to interpret complex micro-energy signals during rock mass failure development under specific failure mechanisms.

Key Words: micro-energy signals; energy evolution; rock mass failure; local mechanical mechanisms

1. Introduction

Heterogeneous materials in slope rock masses produce internal discontinuities and intricate deformation patterns through the interplay of multiple localized mechanical processes, such as the fracturing of intact rock and the sliding of discontinuities. Therefore, the investigation of rock mass deformation and failure must be based on the mechanical behavior of micro-scale or localized structures (Stead and Wolter, 2015; Mas Ivars et al., 2011; Wang et al., 2020). Current methods for assessing rock mass failure development in engineering practice rely primarily on displacement signals. Using only displacement signals may fail to capture important details of the underlying failure mechanisms.

According to the literature, the energy evolution of a rock mass is related to its mechanical mechanisms. The processes of rock deformation and failure development can be modeled in terms of energy input, accumulation, dissipation, and release (Xie et al., 2009; Wasantha et al., 2014; Liu et al., 2024; Deng et al., 2023; Liu et al., 2024). Rock initially undergoes deformation under the effects of external forces during the energy input phase. The total energy input within the rock mass, equivalent to the integral of the stress-strain curve (Xie et al., 2009; Liu et al., 2024), is generally categorized into accumulative energy and dissipative energy (He et al., 2020; Yang et al., 2023; Yu et al., 2023). Accumulative energy stored within the rock matrix exists primarily as strain energy due to the deformation of the specimen. Upon failure, the accumulated energy is released through elastic rebound (Xie et al., 2009; Wasantha et al., 2014; Liu et al., 2024). The released energy is then transferred into the kinetic energy of the separating debris, driving the post-failure mechanical behavior of the rock material (Guo et al., 2020). Under continuous deformation, internal structures within the rock are subject to failure, leading to the release of energy in other forms (e.g., heat), referred to as dissipative energy. This irreversible process is typically accompanied by plastic deformation and rock strength degradation.

According to relevant research, variations in energy accumulation and dissipation trends influence the initiation and propagation of fractures and the development of sliding surfaces within a rock mass. Fractures continue to propagate as long as energy accumulation exceeds dissipation, and rock mass failure occurs when the accumulated energy reaches its ultimate capacity. Therefore, the internal energy partitioning of the rock mass could serve as a basis for assessing failure probability and determining the factor of safety (Das et al., 2023; Guo et al., 2020; Gao et al., 2017; Liu et al., 2024; Li et al., 2017). Furthermore, distinct micro-evolutionary trends lead to variations in

mechanical characteristics at failure and in post-failure morphologies (Das et al., 2023; Xie et al., 2009). Additionally, energy signatures undergo significant changes before and after failure; the pre-failure phase is dominated by energy accumulation, whereas the post-failure phase shifts toward energy dissipation. Thus, the state of the rock mass can be identified through the dominant energy mode (Li et al., 2017; Yan et al., 2019). Research has also shown that the fundamental causes of these differing energy characteristics lie in the internal features of the rock mass, including water content, discontinuity orientation, lithology, and stress states (Liu et al., 2024; Wasantha et al., 2014; Li et al., 2017; Yan et al., 2019).

Previous research has primarily focused on analyzing the total energy within drill cores or numerical models. Total energy is a macroscopic signal; therefore, it cannot directly distinguish the contributions of individual local mechanical mechanisms. However, local mechanical mechanisms have the potential to serve as indicators for analyzing the evolution characteristics of rock mass failure. Therefore, this study establishes a numerical analysis method for localized regions within a rock mass, and defines the energy signals from these localized regions as "micro-energy." A large-scale landslide in Wufeng Township, Hsinchu County, was selected as the study area, and a simplified numerical model was developed based on its failure mechanism. Multiple monitoring points were established at different locations within the model to characterize the local mechanical behaviors and their corresponding micro-energy characteristics. The results indicate that the micro-energy signals within the model exhibit spatial and stage-dependent variations, suggesting their potential for identifying failure zones and assessing the early-stage development of landslides.

2. Methodology

2.1 Concept of Micro-energy

Micro-energy is defined as the energy stored, transferred, released, or dissipated within a local region of a rock mass. Here, "micro" is defined relative to the rock mass as a whole, rather than referring to the molecular level. The analytical scale can be adjusted according to the research objective.

This study employs the Discrete Element Method (using the PFC^{3D} software) to develop a numerical model. Since a PFC^{3D} model is composed of particles, each particle is treated as the unit of analysis for micro-energy signals, with its volume defining the spatial scale of analysis. In practice, rather than recording the micro-energy signals of all particles, multiple representative particles are selected for monitoring. The selected

particles are referred to as monitoring points, and their selection procedure is detailed in Section 2.3. Local mechanical mechanisms may involve multiple energy storage, conversion, and dissipation processes, which can occur simultaneously and interact during rock failure. Elastic deformation leads to strain energy accumulation, which can be released during elastic recovery. Moving objects possess kinetic energy, with translational kinetic energy proportional to the square of velocity. Relative sliding along contact interfaces causes energy dissipation through friction. In addition, vibrations, collisions, and other local motions may involve energy dissipation through damping.

This study employs the linear parallel bond model to construct the numerical models. The micro-energy signals recorded at each monitoring point are obtained exclusively from the monitored particle itself and all contacts associated with it, including their bonding interactions. According to the numerical definitions in PFC^{3D}, the elastic energy stored in linear springs at particle contacts is defined as micro-strain energy, while the elastic energy stored in parallel bonds is defined as micro-bond strain energy. The energy associated with particle translation and rotation is defined as micro-kinetic energy. The energy dissipated through frictional sliding at particle contacts is defined as micro-friction energy, while the energy dissipated through contact damping is defined as micro-damping energy. The five micro-energy components are calculated based on the energy formulations implemented in PFC^{3D}, as follows:

A. Micro-strain energy:

$$E_s = \frac{1}{2}\left(\frac{[k_n \cdot \delta_n]^2}{k_n} + \frac{[k_s \cdot \delta_s]^2}{k_s}\right) \tag{5}$$

where E_s denotes the micro-strain energy; k_n and k_s respectively represent the normal and shear stiffness; and δ_n and δ_s indicate the normal and tangential components of relative displacement.

B. Micro-bond strain energy:

$$E_b = \left(\frac{(k_n A \delta_n)^2}{k_n A} + \frac{(k_s A \delta_s)^2}{k_s A} + \frac{(k_s J \theta_t)^2}{k_s J} + \frac{(k_n I \theta_b)^2}{k_n I}\right) \tag{6}$$

where E_b denotes the micro-bond strain energy; δ_n and δ_s respectively represent the normal and tangential components of relative displacement; θ_b and θ_t are the relative bend and twist rotations; and A, I and J correspond to the cross-sectional area, moment of inertia, and polar moment of inertia of the bond, respectively.

C. Micro-kinetic energy:

$$E_k = \frac{1}{2}mV^2 + \frac{1}{2}I\omega^2 \tag{7}$$

where E_k denotes the micro-kinetic energy; m and V respectively represent the mass and translational velocity; and I and ω correspond to the moment of inertia and angular velocity.

D. Micro-damping energy:

$$E_d = \left[\left(2D_n\sqrt{\frac{m_1 m_2}{m_1+m_2}k_n}\right)V_n + \left(2D_s\sqrt{\frac{m_1 m_2}{m_1+m_2}k_s}\right)V_s\right]\cdot \mathrm{V}\cdot\Delta t \quad (8)$$

where E_d denotes the micro-damping energy; D_n and D_s respectively represent the normal and shear critical damping ratios; V_n and V_s are the normal and tangential components of the relative velocity; k_n and k_s denote the normal and shear stiffness; and m_1 and m_2 correspond to the individual masses of the two colliding particles.

E. Micro-friction energy:

$$E_f = (\mu \cdot N)\cdot \delta_s \quad (9)$$

where E_f denotes the micro-friction energy; and δ_s, μ, and N represent the tangential component of relative displacement, the friction coefficient, and the normal force, respectively.

2.2 Introduction to The Study Area

This study focused on the landslide-prone region in Wufeng Township, Hsinchu County, Taiwan. This site, situated on the right bank of Tuchang Creek (Fig. 1 (b)) covers an area of roughly 13 hectares, characterized by a steep slope oriented toward the North-Northwest. According to previous investigations (Lo and Wu, 2024; Lo and Wu, 2025), Tuchang Creek coincides with an anticline axis that runs roughly parallel to the creek, causing the strata in the study area to dip towards the southeast (N58°E/62°SE), resulting in an anaclinal slope (Fig. 1(a)). The rock mass in the study area is intersected by two prominent sets of diagonal joints with orientations of N19°W/56°SW and N28°W/42°NE, respectively. The lithology comprises sandstone intercalated with argillite, pure sandstone, and interbeds of sandstone and argillite. The bedrock is overlain by a layer of colluvium deposited during historical landslide events, ranging in thickness from 8 - 17 m (Fig. 1(b) and (c)). Previous borehole investigations revealed that the undeformed strata dip at approximately 70° - 90°, with the dips becoming less pronounced near the surface, indicative of toppling deformation. The study area has undergone two large-scale landslides. Satellite imagery reveals rock mass deformation induced by slope-toe erosion prior to the first event, which occurred during Typhoon Aere in 2004. The sliding mass from the initial landslide eroded the toe of the eastern slope, inducing rock mass deformation in that sector. This area

subsequently collapsed following extreme rainfall from Typhoon Saola (2012) and Typhoon Soulik (2013). The toe of an uncollapsed rock mass between the two previous landslide zones is already undergoing erosion and deformation, indicating high susceptibility to failure in the future. Lo and Wu (2024 and 2025) identified deep-seated toppling as the failure mechanism in this study area. The evolution of the landslide is described as follows:

The intense erosion of Tuchang Creek led to the slope toe failure, which in turn significantly exacerbated the rock mass toppling deformation. This led to the pronounced development of tension cracks visible at the slope crest (Fig. 2(a)), along with interlayer slip along discontinuities and the rapid propagation of the slip surface (Fig. 2(b)). This deformation expanded rapidly from the toe toward the crest within a short period (Fig. 3(b)). During the initial stage of toppling deformation, the rock mass within the study area primarily experienced bending and overturning of rock layers, accompanied by interlayer slip. As the deformation continued to evolve, the toppling hinge surface became fully developed (Fig. 3(c)). While the deformation continues to progress, the rock material underwent stress-induced failure, leading to the formation of cracks. These cracks developed along the toppling hinge surface and formed into local sliding surfaces. This process extended progressively from the toe of the slope toward the crest (Fig. 3(d)). In the final stage, a thoroughgoing circular sliding surface eventually formed above the toppling hinge surface, triggering the main rock slide (Fig. 3(e)).

2.3 Model Setup and Experimental Procedures

This study aims to investigate the evolution of local mechanical mechanisms and their associated micro-energy signals within rock masses during failure development. Common local mechanical mechanisms within a rock mass include rock deformation, rock fracturing, and sliding along discontinuities or sliding surfaces. Each of these mechanisms influences the evolution of micro-energy signal in different ways. The failure development of a rock mass typically involves the combined effects of multiple mechanical mechanisms, resulting in complex patterns of micro-energy signal evolution that are difficult to analyze. Therefore, this study first analyzes individual mechanical mechanisms. Their micro-energy signal characteristics are then used as a basis for analyzing micro-energy signals under the combined effects of multiple mechanical mechanisms. In practice, it is difficult to completely isolate individual mechanical mechanisms. Therefore, this study employs experimental methods with relatively controlled loading and boundary conditions to reduce the complexity arising from multiple mechanical mechanisms, thereby establishing conditions in which a specific mechanical mechanism predominates. The analytical framework described

above comprises three numerical models: a uniaxial compression model, a direct shear model, and a simplified slope model, designated as scale 1-a, scale 1-b, and scale 2, respectively. The uniaxial compression test model (scale 1-a) is used to simulate the deformation, damage accumulation, and eventual failure of intact rock under stress. The model is a rock core composed of approximately 9,500 particles, with particle radii ranging from 1 to 1.5 mm (Fig. 4). The lateral surface of the rock core is free, while the top and bottom surfaces are bounded by walls, each moving toward the core at a rate of 15 cm/s. The particle size and loading rate are determined through repeated simulations, progressively reducing each parameter until further reductions produce no significant changes in the simulation results.

The direct shear test model (scale 1-b) is used to simulate sliding along a discontinuity or slip surface under externally applied stress. Scale 1-b consists primarily of approximately 50,000 particles, each with a radius of 1 mm (Fig. 5). The upper and lower portions of the specimen are each enclosed by five walls, forming the upper and lower shear boxes, respectively. The lower box remains fixed, while the upper box moves at a constant rate of 5 mm/s. The displacement rate is determined using the same procedure as the loading rate in scale 1-a. Both the direct shear and uniaxial compression tests involve laboratory experiments and numerical simulations. The laboratory experiments are used to calibrate the numerical models (see Section 2.4), while the numerical models are used to analyze micro-energy signals.

The simplified slope model (scale 2) is constructed based on the deep-seated toppling failure mechanism observed in the study area. This study focuses on the effects of landslide mechanisms on micro-energy signals, while variations caused by changes in topography or stratigraphic thickness are not investigated. The model is a simplified triangular slope composed of particles with a radius of 1.25 m (Fig. 6). Each stratigraphic layer within the slope is 5 m thick, with bedding planes perpendicular to the base of the triangle. The base of the triangle is fixed, while the two inclined sides are free boundaries. The left inclined side serves as the slope face, with its angle relative to the horizontal determined based on the study area.

During the simulation, the mechanical behavior of the model exhibits variations in both time and space. To characterize the mechanical behavior and associated micro-energy signal responses at different stages and locations, the simulation process is divided into several failure development stages. Furthermore, the model is divided into multiple spatial zones based on structural integrity (assessed from the distribution of intact bonds) and mechanical behavior characteristics at the time of macro failure. The

spatial partitioning results for each model are presented in Chapter 3. Each spatial zone of the model contains multiple monitoring points, which are evenly distributed within the zone to capture micro-energy signals at different locations. Furthermore, to ensure a consistent sample size across all zones, the same number of monitoring points is assigned to each. The locations of the monitoring points are determined in two steps. First, spatial zones are identified through simulations without recording micro-energy signals. The monitoring point locations are then determined based on the spatial partitioning results.

2.4 Model Calibration

A process of calibration and comparison was performed to ensure that the mechanical mechanisms represented by the models aligned with actual conditions in the study area. The parameters for scale 1-a are calibrated based on laboratory uniaxial compression test results. Sensitivity analysis indicates that Young's modulus and peak strain are more sensitive to variations in particle and bond stiffness; therefore, they are used to calibrate these stiffness parameters. Meanwhile, peak strength and peak strain are used to calibrate tensile strength, cohesion, and friction angle. In addition, both the normal and shear critical damping ratios are set to 0.7, as adopted in previous quasi-static simulations (Rong et al., 2020; Huang et al., 2025), while the particle density is set to the measured density of the rock core. The calibration results (Fig. 7) show that both the laboratory test and numerical simulation yield a peak strength of 22.91 MPa, with an error of less than 0.1%. The corresponding peak strains are 0.89% and 0.885%, respectively, with an error of approximately 0.6%. The elastic modulus is calculated as the secant slope of the stress–strain curve from the beginning of the simulation to the onset of nonlinear deformation. The values obtained from the laboratory test and numerical simulation are 3050 MPa and 2864 MPa, respectively, with an error of approximately 6.1%. It should be noted that the numerical model employs the linear parallel bond model, whose linear-elastic bond behavior may limit the reproduction of certain nonlinear deformation characteristics. Although incorporating a Discrete Fracture Network (DFN) can improve the simulation of nonlinear behavior, DFN was not included in this study to reduce the number of model variables. Consequently, the agreement between the numerical simulation and laboratory test results may be limited, and relative errors below 10% are considered ideal calibration results in this study. The final micro-parameters for each model are summarized in Table 1.

In scale 1-b, particle and bond stiffness are calibrated based on the shear stiffness and peak shear displacement obtained from direct shear tests. Tensile strength, cohesion,

friction angle, and friction coefficient are calibrated based on the peak shear strength. The normal and shear critical damping ratios and particle density are determined using the same methods as those in scale 1-a.

Since scale 2 lacks quantitative reference data for calibration, its parameters are calibrated through parameter conversion and qualitative comparison. According to Potyondy and Cundall (2004), the relationship between particle stiffness and Young's modulus can be expressed by the following equation:

$$k_{particle} = n \times R \times E \tag{10}$$

Here, n is a constant related to the material properties. For each new material, n must be determined through parameter calibration based on laboratory test results. R and E represent the particle radius and the Young's modulus of the model, respectively. The relationship between bond stiffness and Young's modulus is given as follows:

$$k_{bond} = n \times \frac{E}{L} \tag{11}$$

Here, n is a constant, E is Young's modulus, and L is the bond length, taken as twice the particle radius for the particles.

In this study, the values of n in the formulas are determined based on the calibration results of scale 1-a and scale 1-b. The particle radius of scale 2 is then substituted into the formulas to calculate the stiffness values. These values serve as the initial settings for the second stage of calibration, while the remaining parameters are initially assigned values from scale 1-a and scale 1-b. During the second phase of calibration, a simulation is first conducted using the initial parameter settings. The simulated landslide mechanism is then compared with the actual landslide mechanism observed in the study area to guide parameter adjustments, which are repeated until the model adequately reproduces the observed mechanism. Stiffness primarily influences the development of column bending, while tensile strength, cohesion, and friction angle determine whether the landslide mechanism transitions from simple flexural toppling to deep-seated toppling. The critical damping ratio and friction coefficient are associated with local failure propagation and interlayer slip, respectively. Particle density is set to match the measured density of the rock core.

2.5 Signal Analysis Methods

To standardize the horizontal-axis scales across models, the time or shear displacement at macro failure is used as the reference value for each model. The corresponding horizontal-axis values are then divided by this reference value to obtain

dimensionless coordinates. Data for each micro-energy type are divided into multiple analysis units based on failure development stages and spatial zones. Each analysis unit contains micro-energy series from multiple monitoring points. Multiple methods are employed to analyze the analysis units, including slope threshold, normalized energy growth rate, Yamamoto mutation index, peak ratio, and RBF dissimilarity. These methods are classified into two categories: stage-based indicators and stage-transition indicators. Stage-based indicators characterize signal features within a single stage and are calculated using data from that stage. These include slope threshold, normalized energy growth rate, and RBF dissimilarity. Stage-transition indicators compare analysis units from two adjacent stages within the same spatial zone to assess differences between the stages. These include Yamamoto mutation index and peak ratio. For each method, an indicator value is first calculated at each monitoring point. The indicator values from monitoring points within the same spatial zone are then summarized by their minimum and maximum original values. Each statistical method is described in detail below:

1. slope threshold:

This method first determines the linear regression equation for the selected data. The absolute value of the regression slope is then calculated and compared with predefined thresholds. The magnitude of this value represents the rate of change in the energy signal. Values below the first threshold of 1.1 indicate low signal variation, while values above the second threshold of 4 indicate extremely rapid signal variation. Values between the two thresholds indicate rapid signal variation. The linear regression equation is given as follows:

$$f(t) = a + bt \tag{12}$$

Here, a is a constant, t represents time, and b is the slope.

2. normalized energy growth rate:

This method characterizes the relative rate of change in a signal by dividing the derivative of energy by the corresponding energy value, thereby eliminating the energy dimension. It can highlight variations in micro-energy signals even when their magnitudes are small. The absolute value of the calculated indicator is used for classification, regardless of the direction of signal variation. The normalized energy growth rate indicator is classified into three levels: low

variation, rapid variation, and extremely rapid variation, corresponding to ranges of 0–0.7, 0.7–6, and greater than 6, respectively.

$$N = \frac{1}{n}\sum_{i=1}^{n}\frac{1}{E_i}\frac{dE}{dt}\Big|_{t=i} \tag{13}$$

Here, n is the total number of data points in the micro-energy series for the given stage, E_i is the micro-energy value of the i-th data point, and $\frac{dE}{dt}$ is the derivative of micro-energy with respect to time.

3. Yamamoto mutation index:

The Yamamoto mutation index is used to analyze differences in mean energy intensity between two adjacent stages. The index values are classified into three levels: low variation, moderate variation, and high variation, corresponding to ranges of 0–0.5, 0.5–1.1, and greater than 1.1, respectively. The formula is given as follows:

$$Y = \frac{|\mu_i - \mu_{i-1}|}{\sigma_i + \sigma_{i-1}} \tag{14}$$

Here, μ_{i-1} and σ_{i-1} represent the mean and standard deviation of the micro-energy signal in the preceding stage, respectively, while μ_i and σ_i represent those in the subsequent stage.

4. peak ratio:

The peak ratio compares the maximum signal values between adjacent stages, making it suitable for identifying stages in which micro-energy signals undergo rapid changes. A peak ratio greater than 1 indicates an increase in the maximum micro-energy value. Values between 1 and 1.25 indicate a slight increase, values between 1.25 and 4 indicate a moderate increase, and values greater than 4 indicate a sharp increase. A peak ratio less than 1 indicates a decrease in the maximum micro-energy value, classified into three levels: slight, moderate, and sharp decreases, corresponding to ranges of 1–0.8, 0.8–0.25, and less than 0.25, respectively. The formula for the peak ratio is given as follows:

$$P = \frac{M_i}{M_{i-1}} \tag{15}$$

Here, M_i and M_{i-1} represent the maximum micro-energy signal values in the subsequent and preceding stages, respectively.

5. RBF dissimilarity:

RBF dissimilarity is used to characterize the degree of dissimilarity among all data points within a micro-energy series of specific analysis unit. A higher value indicates greater dissimilarity among signal values, which may be associated with rapid increases or decreases or irregular fluctuations in the micro-energy signal within a given stage. RBF dissimilarity is classified into three levels: low, moderate, and high dissimilarity, corresponding to ranges of 0–0.1, 0.1–0.8, and greater than 0.8, respectively. The formula is given as follows:

$$D = \frac{2}{n(n-1)} \sum_{i=1}^{n-1} \sum_{j=i+1}^{n} \left[1 - exp\left(-\gamma\left(z_i - z_j\right)^2\right)\right] \tag{16}$$

Here, n is the total number of data points in the micro-energy series for the given stage, and γ is a sensitivity parameter. This parameter is manually specified and influences the sensitivity of RBF dissimilarity to small differences in signal values. z_i and z_j represent standardized data values. The formula for standardization is given as follows:

$$z_i = \frac{E_i - \mu}{\sigma} \tag{17}$$

Here, E_i represents the micro-energy value of the i-th data point, while μ and σ represent the mean and standard deviation of all micro-energy values within the micro-energy series, respectively.

3. Results

Scale 1-a is divided into two spatial zones: Near the failure plane and Far from the failure plane. The failure development process is divided into four stages based on the mechanical characteristics described by Martin and Chandler (1994), as identified through changes in the number of intact bonds and the stress–strain curve. These stages

include crack closure phase, linear elasticity, stable crack growth, and unstable crack growth, hereafter referred to as stage i through stage iv, respectively. During stage i, particles become more tightly packed as existing gaps are compressed, with only 0.2% of the bonds breaking. During stage ii, the stress–strain curve exhibits a linear increase, and 95.4% of the bonds remain intact at the end of this stage. During stage iii, the proportion of intact bonds steadily decreases, and the stress–strain curve exhibits nonlinear behavior. By the end of this stage, 72.0% of the bonds remain intact. During stage iv, the number of intact bonds drops sharply to 39.3% of the initial value. Furthermore, cracks formed by bond breakage coalesce, leading to the formation of a failure plane extending across the model.

Beginning in stage ii, the maximum slope values of micro-strain energy and micro-bond strain energy reach 2.92 and 2.91, respectively (Fig. 8(a) and (b)). Although the maximum slope value of micro-damping energy is only 4.10×10^{-2}, its maximum normalized energy growth rate reaches 2.26 (Fig. 8(d)). These results indicate that micro-damping energy exhibits an increasing trend despite its relatively low growth rate. During stage iii, the RBF dissimilarity of micro-damping energy near the failure plane reaches 6.93×10^{-1}, while its slope values span three classification levels, ranging from 2.69×10^{-1} to 4.17. The distribution of indicator values across multiple classification levels reflects differences among monitoring points within the same spatial zone. This suggests irregular local perturbations, consistent with the mechanical characteristics of local bond breakage. During stage iii, the maximum slope value of micro-kinetic energy near the failure plane reaches 1.44 (classified as rapid variation), higher than the 8.09×10^{-1} (classified as low) observed far from the failure plane (Fig. 8(e)). However, the most significant change in micro-kinetic energy occurs during stage iv, when the slope range shifts from -3.46×10^{-1}–1.44 in stage iii to $3.06–6.60 \times 10^{1}$. This indicates that micro-kinetic energy exhibits an increasing trend at all monitoring points, with extremely rapid growth at many of them. Furthermore, during stage iv, the slope ranges for micro-strain energy and micro-bond strain energy are -1.36×10^{1} to 1.50×10^{1} and -3.45×10^{1} to 1.19×10^{1}, respectively. These results indicate substantial differences among monitoring points, with individual micro-energy signals exhibiting either extremely rapid increases or decreases (Fig. 8(a) and (b)).

Scale 1-b is divided into two spatial zones: Near the sliding surface and Far from the sliding surface. The failure development process is divided into five stages based on the mechanical characteristics described by Zhu et al. (2019), as identified through the sliding behavior along the sliding surface, changes in the number of intact bonds near the sliding surface, and changes in the shear stress–shear displacement curve.

These stages include linear elastic, nonlinear hardening, peak shear stress, progressive softening, and stable sliding, hereafter referred to as stage i through stage v, respectively. During stage i, no relative sliding occurs along the sliding surface because the particles on either side remain interlocked. During stage ii, progressive bond breakage disrupts the existing interlocking, resulting in nonlinear behavior in the shear stress−shear displacement curve. By the end of this stage, relative sliding has begun along the sliding surface. During stage iii, the model reaches its peak shear stress. During stage iv, continued sliding leads to repeated interlocking–sliding–unlocking cycles among particles. Furthermore, relative sliding causes continued bond breakage near the sliding surface. During stage v, the model enters a state of stable sliding.

During stage i, the slope values of micro-bond strain energy exhibit spatial differences (Fig. 9(b)). Notably, the maximum slope value near the sliding surface reaches 3.4465×10^{1}, indicating greater bond deformation near the sliding surface. During stage ii, the indicators continue to show more pronounced changes near the sliding surface. Notably, the minimum peak ratio of micro-bond strain energy between stage ii and stage iii is 0 (Fig. 9(b)), indicating that the energy signal drops to zero by the end of stage ii and remains at zero throughout stage iii, a characteristic response to bond breakage. Meanwhile, the maximum and minimum slope values of micro-damping energy are 7.96 and 4.27×10^{-3}, respectively, spanning three classification levels from low variation to extremely rapid variation (Fig. 9(d)). Micro-damping energy is associated with disturbances caused by bond breakage and the loss of interlocking. The substantial difference between the maximum and minimum slope values indicates nonuniform responses among monitoring points. During stage iii, the maximum slope value of micro-damping energy decreases to 6.00×10^{-1}. The maximum normalized energy growth rate of micro-friction energy rises to 3.97 (Fig. 9(c)), indicating an increasing trend consistent with the onset of sliding. This sliding behavior is also reflected in micro-kinetic energy (Fig. 9(e)), with its Yamamoto mutation index increasing to 1.32. During stage iv, the maximum slope value of micro-friction energy near the sliding surface increases to 1.67 (Fig. 9(c)), indicating a rapid increasing trend that persists into stage v. In contrast, the maximum slope value far from the sliding surface is only 1.12×10^{-4}, indicating that an increase in micro-friction energy is a key characteristic of sliding. Meanwhile, micro-strain energy near the sliding surface exhibits high variability, with a maximum RBF dissimilarity of 9.34×10^{-1}, consistent with the repeated interlocking–sliding–unlocking cycles (Fig. 9(a)). The stepwise changes in micro-friction energy and micro-damping energy are also associated with this mechanical mechanism (Fig. 9(c) and (d)).

Scale 2 is divided into three spatial zones: In the sliding mass, Near the sliding surface, and Non-failure rock mass. The failure development process is divided into four stages based on the characteristics of deep-seated toppling: bending of rock layers (Fig. 3(a) to (c)), crack development (Fig. 3(d)), main rock sliding (Fig. 3(e) and (f)), and temporary stability, hereafter referred to as stage i through stage iv, respectively. During stage i, bonds between rock layers continue to break, leading to relative sliding between the layers. During stage ii, bonds within the rock layers themselves also begin to break. During stage iii, the formation of a sliding surface causes the sliding mass to move, and during stage iv, the model reaches a temporarily stable state.

During stage i, the maximum slope values of micro-friction energy and micro-damping energy are 6.13×10^{-1} and 1.11×10^{-1}, respectively, indicating relatively low growth rates for both (Fig. 10(c) and (d)). However, their maximum normalized energy growth rates reach 1.06×10^{8} and 1.74×10^{6}, respectively, indicating that both micro-energy signals have begun to increase without substantial movement of the rock mass as a whole. Meanwhile, the RBF dissimilarity of micro-strain energy in the sliding mass reaches 8.23×10^{-1} (classified as high dissimilarity), consistent with changes in the distribution of forces during interlayer slip (Fig. 10(a)). Between stage i and stage ii, the maximum peak ratio of micro-bond strain energy near the sliding surface reaches 4.50×10^{1} (Fig. 10(b)). In contrast, between stage ii and stage iii, all peak ratio values of micro-bond strain energy in the same zone are below 1, with a minimum of 0.21, indicating a sharp decrease in the maximum energy values. The rapid increase and subsequent decrease in micro-bond strain energy, without reaching zero, suggest that some bonds undergo rapid deformation followed by breakage during stage ii. The same mechanical behavior also contributes to the maximum peak ratio of micro-damping energy reaching 4.45×10^{2} between stage i and stage ii (Fig. 10(d)). Between stage ii and stage iii, the maximum peak ratios of micro-friction energy within the sliding mass and near the sliding surface are 4.57 and 6.46, respectively (Fig. 10(c)). Meanwhile, the maximum peak ratio of micro-damping energy reaches 2.82×10^{1} (Fig. 10(d)). The simultaneous sharp increases in these two types of micro-energy reflect the sliding and fragmentation of the sliding mass, as well as interactions among the fragments. During stage iii, the minimum RBF dissimilarity of micro-bond strain energy near the sliding surface reaches 8.07×10^{-1} (Fig. 10(b)), indicating that the signals at all monitoring points exhibit high dissimilarity, reflecting the extreme instability near the sliding surface during macro failure.

4. Conclusions

Through local monitoring and the analysis of micro-energy signals, this study identifies significant differences in micro-energy characteristics across different failure development stages and spatial zones. By integrating the mechanical behaviors and micro-energy characteristics observed at each stage in scale 1-a and scale 1-b, the results demonstrate that different mechanical behaviors exhibit distinct micro-energy characteristics.

Increasing trends in micro-strain energy and micro-bond strain energy are associated with deformation accumulation, while a sharp decrease in micro-bond strain energy is closely related to bond breakage. An increase in micro-friction energy is associated with local sliding or sliding following macro failure. An increase in micro-damping energy is associated with disturbances caused by bond breakage and changes in the particle interlocking state during sliding. An increase in micro-kinetic energy reflects enhanced local motion, with more pronounced growth commonly observed during the transition to macro failure and in the subsequent stages. Furthermore, the results show that continuous changes in mechanical behavior can be accompanied by higher RBF dissimilarity, while spatial differences in mechanical responses within the same zone can be reflected in wider ranges of indicator values. Together with the mechanical characteristics of each stage, these features can help identify local instability and nonuniform deformation.

The relationships between mechanical behaviors and micro-energy characteristics help interpret the complex micro-energy signals associated with landslide mechanisms, as demonstrated by the results of scale 2. The mechanical behaviors in scale 2 are more complex, exhibiting more diverse stage-dependent and spatial characteristics. These characteristics help distinguish differences among stages and spatial zones but also make micro-energy signals more difficult to interpret. Notably, many of these micro-energy characteristics are similar to those observed in scale 1-a and scale 1-b under specific mechanical behaviors. Therefore, the complementary analysis of the three models enables a more detailed interpretation of micro-energy trends during failure development in rock masses affected by specific landslide mechanisms.

Acknowledgments

The research was mainly supported by National Science and Technology Council, Grant no. NSTC 112-2625-M-A49-002. The authors would also like to thank Prof. Ming-Lang Lin for the advice and assistance provided with this study.

Conflicts of interests

A. To the best of our knowledge, the named authors have no conflict of interest, financial or otherwise.

B. All authors have declare that: (i) no support, financial or otherwise, has been received from any organization that may have an interest in the submitted work; and (ii) there are no other relationships or activities that could appear to have influenced the submitted work.

References

1. Federico, M. Popescu, G. Elia, C. Fidelibus, G. Interno` and A. Murianni, 2012. Prediction of time to slope failure: a general framework. Environmental Earth Sciences, 66, 245-256.
2. Arka Jyoti Das, Prabhat Kumar Mandal, Nilabjendu Ghosh, Awanindra Pratap Singh, Ranjan Kumar, Subhashish Tewari, Rana Bhattacharjee, 2023. Evaluation of energy accumulation, strain burst potential and stability of rock mass during underground extraction of a highly stressed coal seam under massive strata-a field study, Engineering Geology, 322,107178.
3. C.D. Martin and N.A. Chandler, 1994. The progressive fracture of Lac du Bonnet granite, International Journal of Rock Mechanics and Mining Sciences and Geomechanics Abstracts, 31 (6), 643-659.
4. Diyuan Li, Zhi Sun, Tao Xie, Xibing Li, P.G. Ranjith, 2017. Energy evolution characteristics of hard rock during triaxial failure with different loading and unloading paths, Engineering Geology, 228, 270-281.
5. D.O. Potyondy and P.A. Cundall, 2004. A bonded-particle model for rock, International Journal of Rock Mechanics and Mining Sciences, 41(8), 1329-1364.
6. Daping Tai, Shengwen Qi, Bowen Zheng, Chonglang Wang, Songfeng Guo, Guangming Luo, 2022. Shear mechanical properties and energy evolution of rock-

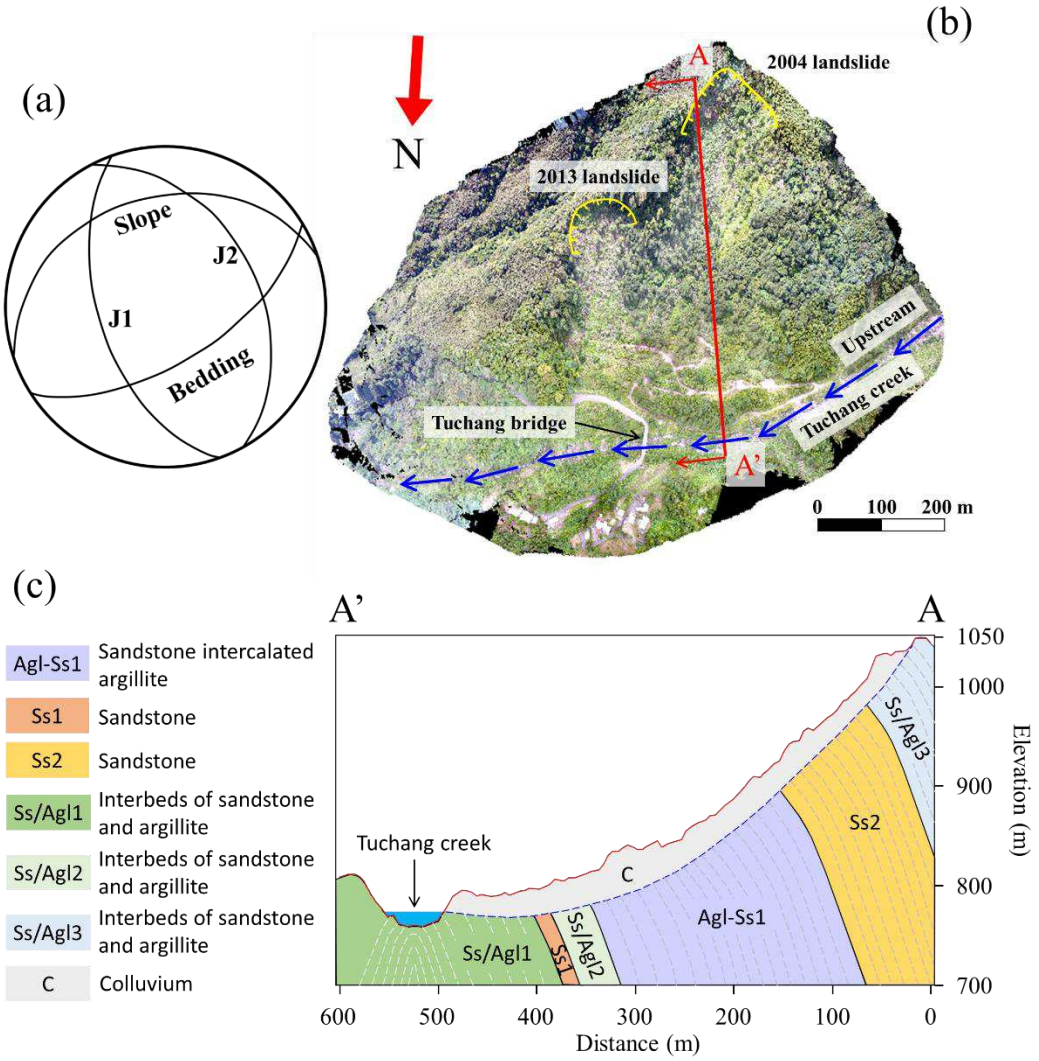
like samples containing multiple combinations of non-persistent joints, Journal of Rock Mechanics and Geotechnical Engineering, 15(7), 1651-1670.
7. Diego Mas Ivars, Matthew E. Pierce, Caroline Darcel, Juan Reyes-Montes, David O. Potyondy, R. Paul Young, Peter A. Cundall, 2011. The synthetic rock mass approach for jointed rock mass modelling, International Journal of Rock Mechanics and Mining Sciences, 48(2),219-244.
8. Doug Stead and Andrea Wolter, 2015. A critical review of rock slope failure mechanisms: The importance of structural geology, Journal of Structural Geology, 74, 1-23.
9. Evert Hoek and Edwin T. Brown, 1980. Empirical strength criterion for rock masses, Journal of the Geotechnical Engineering, 106, 1013-1035.
10. Hoek E, 1983. Strength of jointed rock masses, Geotechnique, 33(3), 187–223.
11. Heping Xie, Liyun Li, Ruidong Peng and Yang Ju, 2009. Energy analysis and criteria for structural failure of rocks, Journal of Rock Mechanics and Geotechnical Engineering, 1 (1), 11–20.
12. Jonny Sjöberg, 2001. Failure Mechanisms for High Slopes in Hard Rock, Slope Stability in Surface Mining, 71-80.
13. Jianbo Zhu, Hua Li and Deng Jh, 2019. A One-Dimensional Elastoplastic Model for Capturing the Nonlinear Shear Behaviour of Joints with Triangular Asperities Based on Direct Shear Tests, Rock Mechanics and Rock Engineering, 52(6), 1671-1687.
14. Leibo Song, Gang Wang, Xingkai Wang, Mingzhi Huang, Kun Xu, Guansheng Han and Guangjian Liu, 2022. The Influence of Joint Inclination and Opening Width on Fracture Characteristics of Granite under Triaxial Compression, International Journal of Geomechanics, 22(5), 1-11.
15. Liangfu Xie, Qingyang Zhu, Yongjun Qin, Jianhu Wang and Jiangu Qian, 2020. Study on Evolutionary Characteristics of Toppling Deformation of Anti-Dip Bank Slope Based on Energy Field, Sustainability 2020, 12(18), 7544.
16. Chia-Ming Lo and Yu-Chen Wu, 2024. Evolution of large-scale landslide at Tuchang creek, Taiwan, EGU General Assembly 2024, Vienna, Austria, 2024, 1.
17. Chia-Ming Lo and Yu-Chen Wu, 2025. Study on the landslide mechanism, monitoring, and scenario simulation of slate slopes caused by adjacent anticline structure, EGU General Assembly 2025, Vienna, Austria, 2025, 1.
18. Dan Huang, Guoyu Wei, Zilong Xiao and Qingping Jin, 2026. A numerical study of the mechanical properties and rock bridge coalescence of discrete distribution jointed rock masses under uniaxial loading, Scientific Reports, 16, 310.

19. Haoyu Rong, Guichen Li, Dongxu Liang, Changlun Sun, Suhui Zhang and Yuantian Sun, 2020. Numerical Investigation on the Evolution of Mechanical Properties of Rock Affected by Micro-Parameters, Applied Sciences, 10(14), 4957.
20. M. M. He, F. Pang, H. T. Wang, J. W. Zhu 3 and Y. S. Chen, 2020. Energy Dissipation-Based Method for Strength Determination of Rock under Uniaxial Compression, Shock and vibration, 2020(1), 1-13.
21. Martin Krkač, Drago Špoljarić, Sanja Bernat and Snježana Mihalić Arbanas, 2016. Method for prediction of landslide movements based on random forests, Landslides, 14, 947-960.
22. P.L.P. Wasantha, P.G. Ranjith, S.S. Shao, 2014. Energy monitoring and analysis during deformation of bedded-sandstone: Use of acoustic emission, Ultrasonics, 54, 217–226.
23. Qifeng Guo, Jiliang Pan, Meifeng Cai and Ying Zhang, 2020. Analysis of Progressive Failure Mechanism of Rock Slope with Locked Section Based on Energy Theory, Energies, 13(5), 1-18.
24. Taoying Liu, Min Tang, Ping Cao, Mengyuan Cui and Longjun Dong, 2025. Shear Energy Evolution and Fracture Behavior of Rock–Concrete Interfaces Under Different Stress-Level Conditions, Materials 2025, 18(4), 795.
25. Wei Gao, Shuang Dai, Ting Xiao and Tianyang He, 2017. Failure process of rock slopes with cracks based on the fracture mechanics method, Engineering Geology, 231,190-199.
26. Xiao Wang, Wei Yuan, Yatao Yan and Xue Zhang, 2020. Scale effect of mechanical properties of jointed rock mass: A numerical study based on particle flow code, 21(3), 259-268.
27. Yan Zhang, Xia-Ting Feng, Xiwei Zhang, Zhaofeng Wang, Mostafa Sharifzadeh, Chengxiang Yang, Rui Kong, Jun Zhao, 2019. Strain energy evolution characteristics and mechanisms of hard rocks under true triaxial compression, Engineering Geology, 260, 105222.
28. Yonghong Liu, Fujun Zhao, Qiuhong Wu, Baojie Fan and Zhenqi Tang, 2024. Experimental Research on Energy Evolution of Sandstone with Different Moisture Content under Uniaxial Compression, Sustainability, 16(11), 1-12.
29. Yang Hao, Yu Wu, Ruoyu Cui, Kewang Cao, Dongdong Niu and Chunhui Liu, 2023. Strain Energy Dissipation Characteristics and Neural Network Model during Uniaxial Cyclic Loading and Unloading of Dry and Saturated Sandstone, Minerals, 13(2), 131-152.
30. Yongjiang Yu, Yuntao Yang, Jingjing Liu, Pengbo Wang, Jiaming Liu, Zhiyuan Song and Shangqing Zhao, 2023. Mechanical characteristics and energy evolution in a rock mass with a weak structural plane, Scientific Reports, 13(1), 1-10.

632 Table. 1 Material parameters for each model

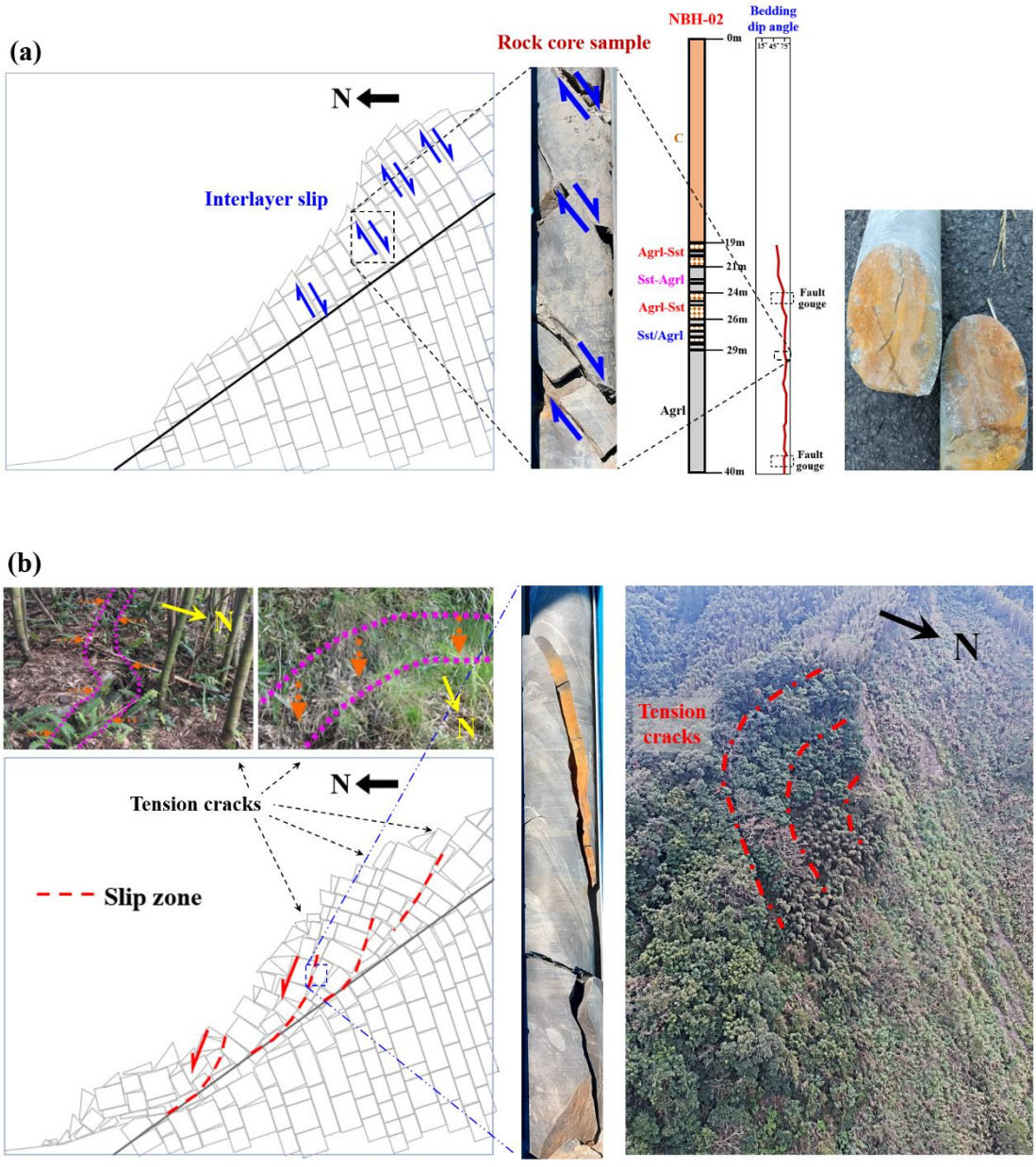
Parameter	Scale1-a	Scale1-b	Scale2	
			Intact rock	Weak plane
particle normal stiffness k_n (N/m)	4.85×10^6	3.40×10^4	5×10^7	5×10^7
particle shear stiffness k_s (N/m)	4.85×10^6	3.40×10^4	5×10^7	5×10^7
bond normal stiffness $(k_{bond})_n$ (N/m)	6.06×10^{11}	4.25×10^9	4×10^6	4×10^6
bond shear stiffness $(k_{bond})_s$ (N/m)	6.06×10^{11}	4.25×10^9	4×10^6	4×10^6
tensile strength (N/m^2)	1.7×10^6	8.0×10^4	1.2×10^6	3.0×10^5
cohesion (N/m^2)	5.0×10^9	8.0×10^4	4.0×10^5	7.0×10^4
friction angle (degrees)	45	0	40	10
critical damping ratio β	0.5	0.5	0.7	0.7
friction coefficient μ	0.577	0.577	0.5	0.5
particle density (kg/m^3)	2500	2710	2600	2600

633
634



635

636 Fig. 1 Distribution of borehole locations and a stratigraphic profile of the study
637 area
638



639

640

641 Fig. 2 Comparison of deformation landforms and underground slip surface
642 characteristics across different zones of the study area: (a) Toppling deformation of the
643 rock mass resulting in flexural toppling/interlayer slip and evidence of subsurface
644 interlayer slip at a depth of 29 meters; (b) Distribution of tension cracks at the slope
645 crest and development characteristics of the slip surface, as identified through field
646 investigation and borehole drilling.
647

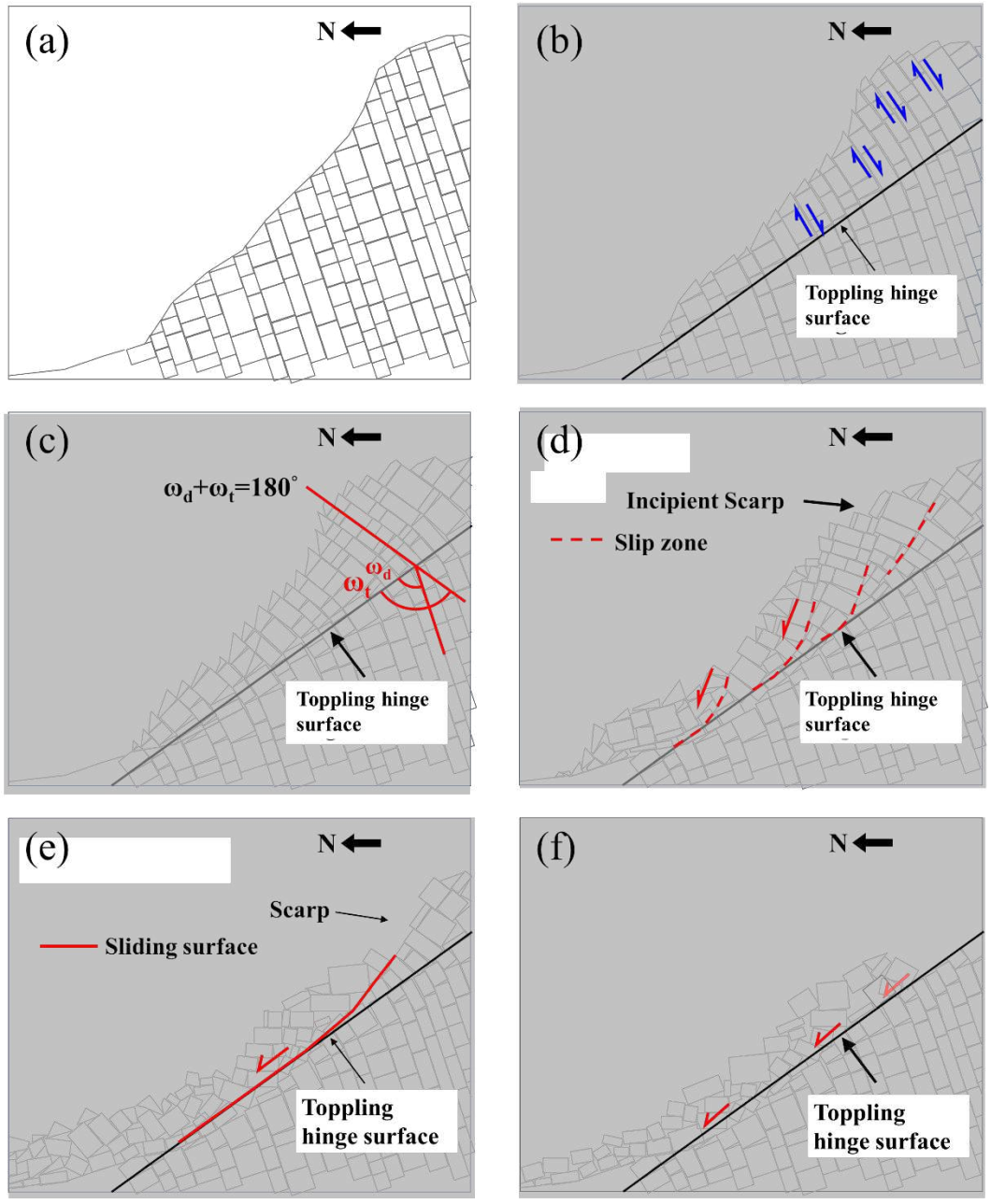
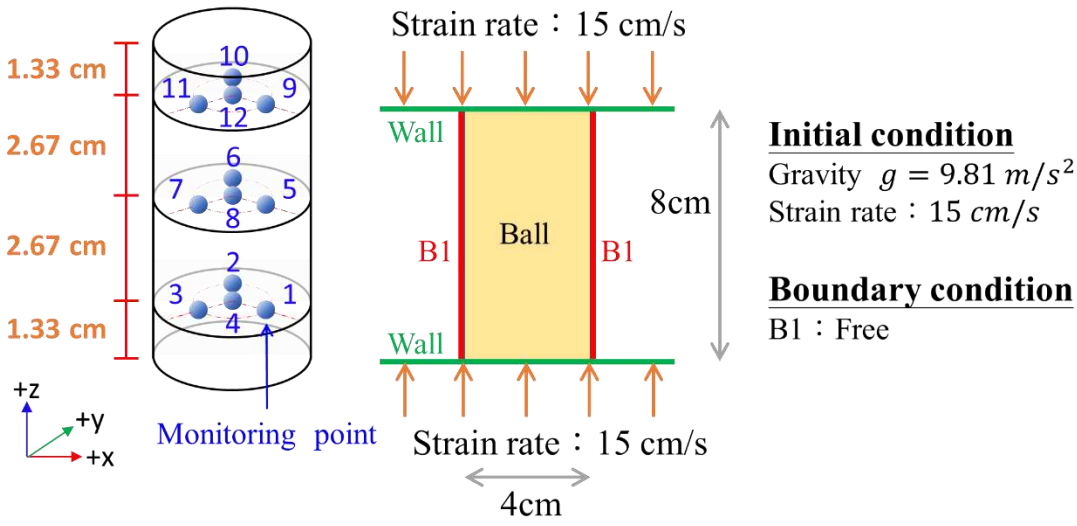


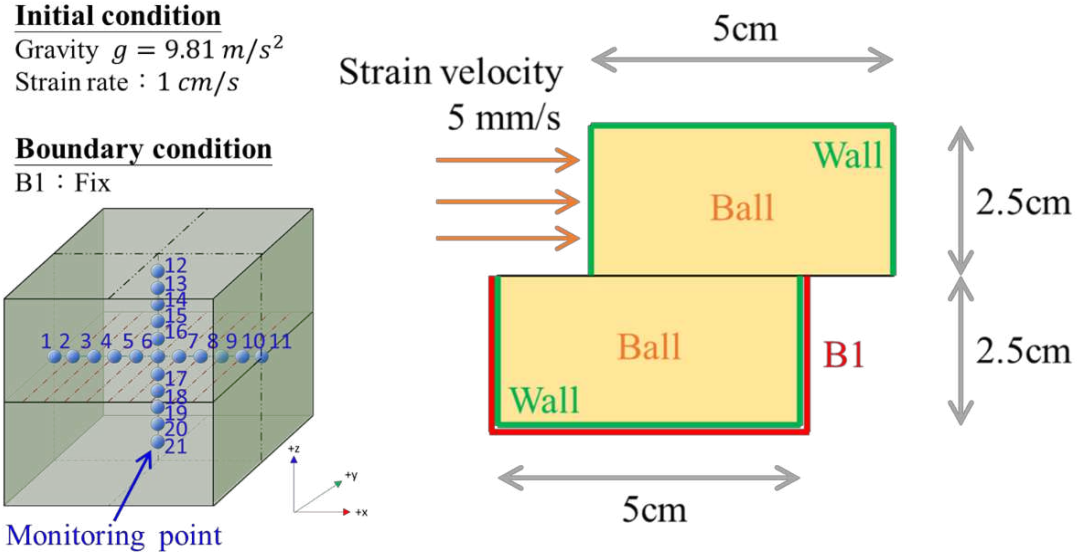
Fig. 3 Evolution of deep-seated toppling landslide in the study area



652

653 Fig. 4 Schematic diagram of the scale1-a model and its monitoring points

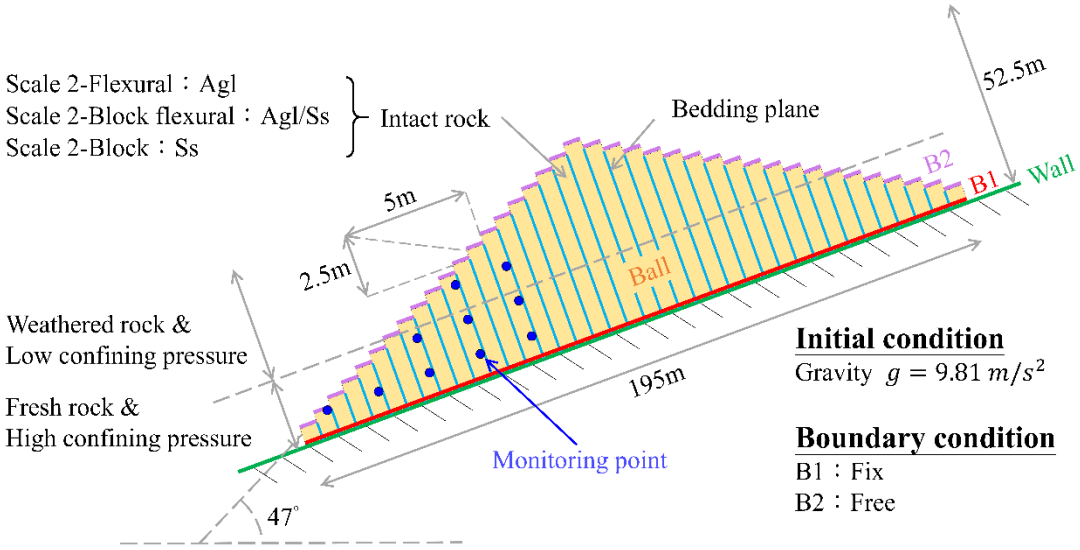
654



655

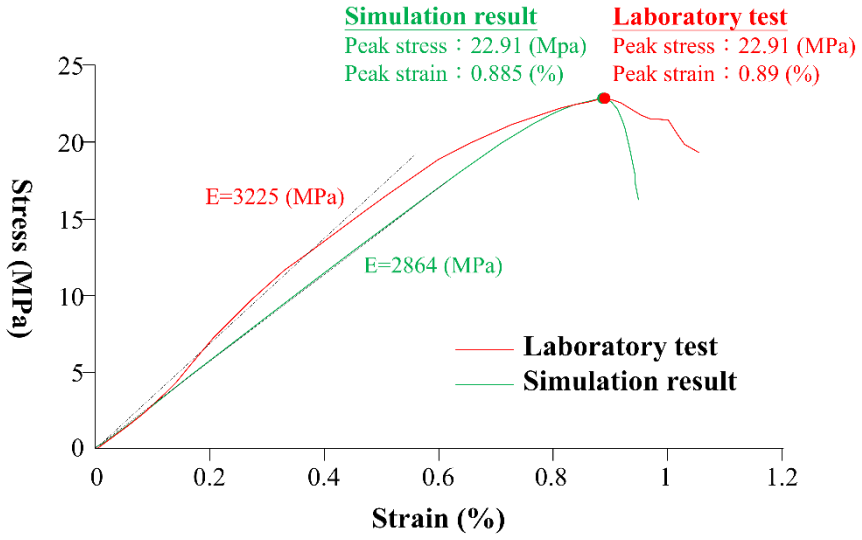
656 Fig. 5 Schematic diagram of the scale1-b model and its monitoring points

657



658

659 Fig. 6 Schematic diagram of the scale 2 model and its monitoring points



660

661 Fig. 7 Simulation and laboratory results of scale 1-a model

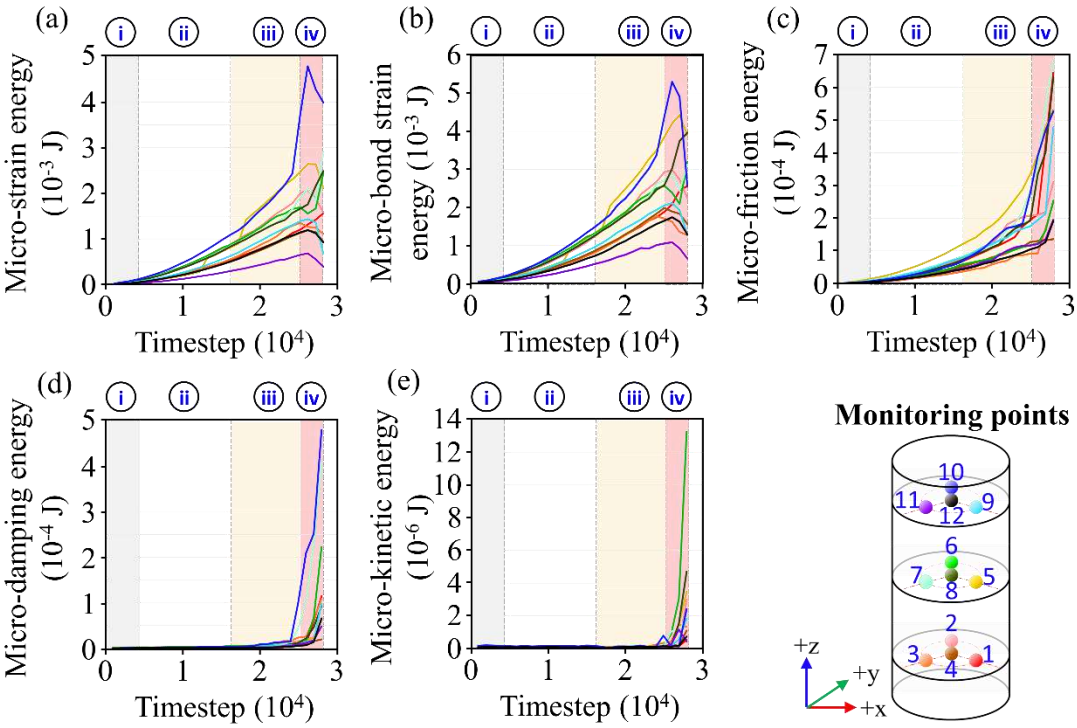
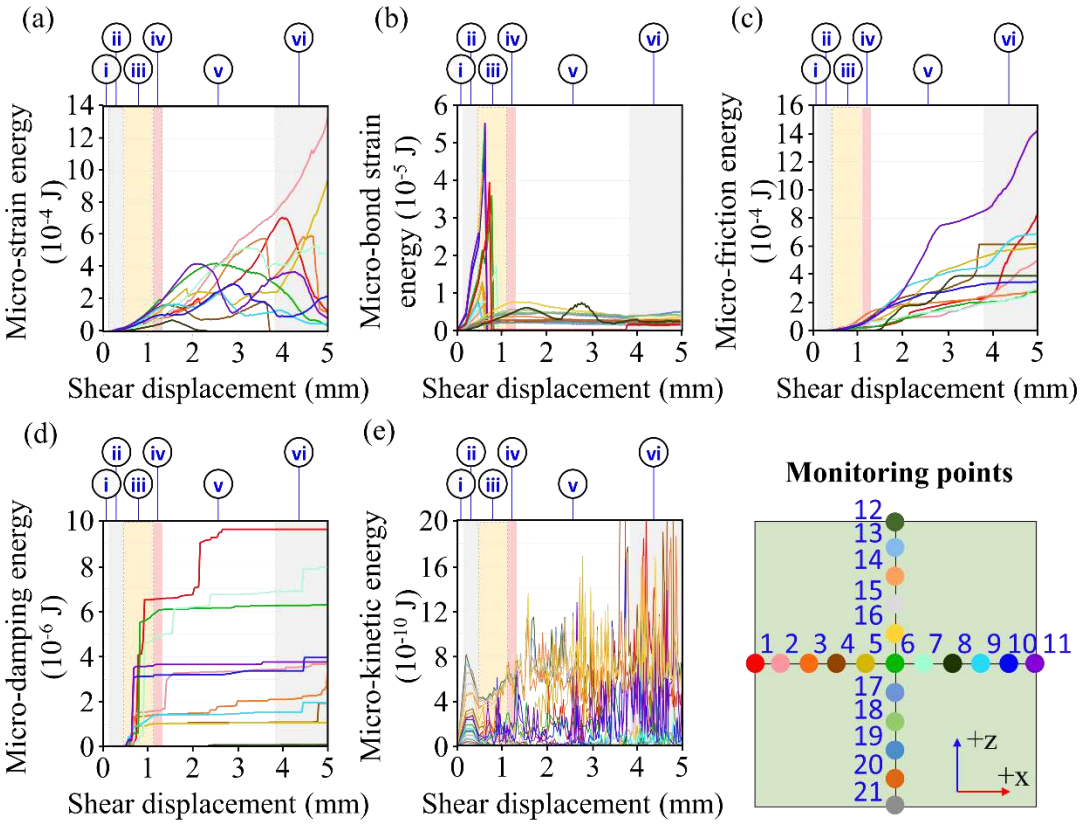


Fig. 8 Monitoring results of the five types of micro energy at scale 1-a monitoring points



666

667 Fig. 9 Monitoring results of the five types of micro energy at scale 1-b
668 monitoring points
669

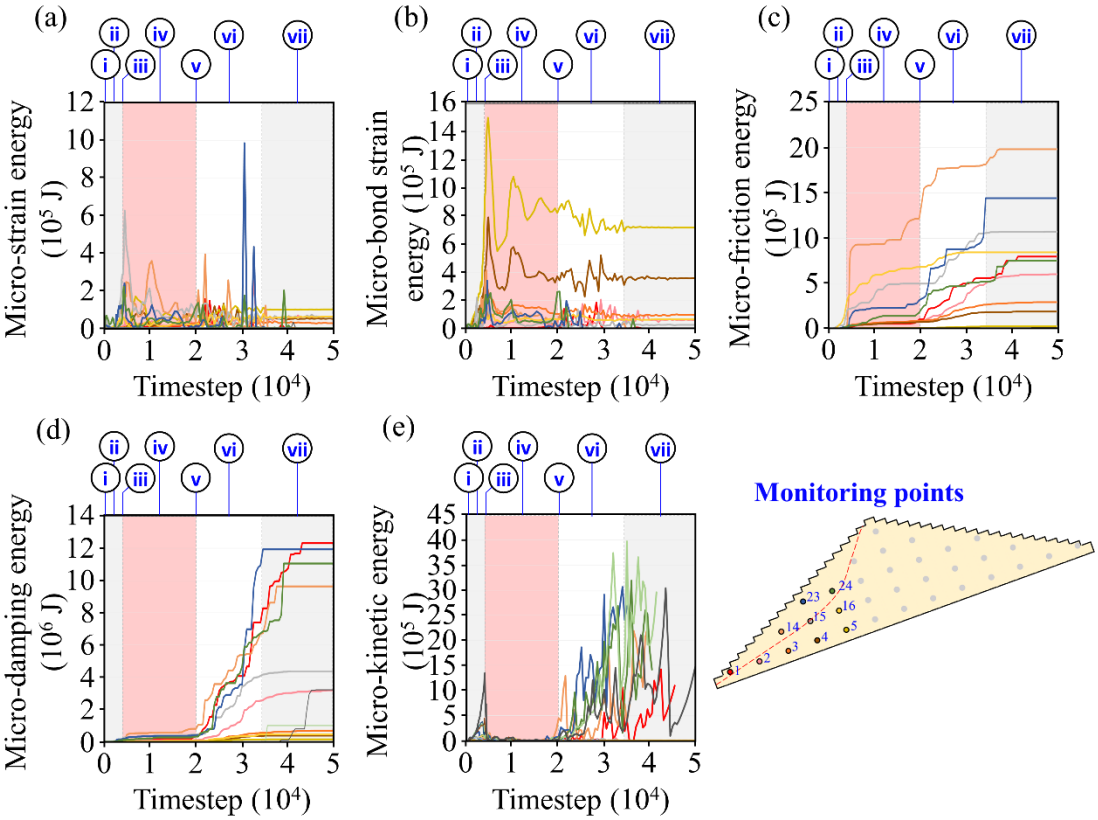


Fig. 10 Monitoring results of the five types of micro energy at scale2 monitoring points